NUCL SCI TECH (2021) 32:97
https://doi.org/10.1007/s41365-021-00925-8

Design optimization and cold RF test of a 2.6-cell cryogenic RF gun

Cheng Wang[1,2,3] · Jian-Hao Tan[3] · Xiao-Xia Huang[3] · Yi-Xing Lu[1,2] · Lin Wang[1,2] · Wen-Cheng Fang[3] · Zhen-Tang Zhao[3]

Received: 7 March 2021 / Revised: 6 July 2021 / Accepted: 8 July 2021 / Published online: 8 September 2021

Abstract To further improve the performance of accelerators, the first cryogenic normal-conducting RF gun in China was designed and manufactured. As a new and attractive trend, this optimized cryogenic RF gun can generate a low-emittance beam with a short-driven laser pulse because of its promising high gradient on the cathode. In this paper, optimization of the RF design and beam dynamics, including suppression of the peak RF field and elimination of the multipole mode, is presented. In addition, the emittance growth caused by the alignment deviation and RF jitter is discussed. After the gun was manufactured, a cold test was conducted at both room temperature and cryogenic conditions. At room temperature, the field distribution was obtained by the bead pull method. Under cryogenic conditions, the RF properties, such as the coupling coefficient and quality factor, varied with temperature. The test results agreed with the design. In the cryogenic test, vibration measurements were performed. Without vibration isolation, a maximum vibration of 50 μm was observed. These cold test results are the basis of the following high-power test.

Keywords Photoinjector · Cryogenic structure · C-band · Cold test

1 Introduction

A photoinjector is one of the most important components of an accelerator. In the last three decades, the exploration of photoinjectors has driven the development of instruments based on accelerators, such as free electron lasers [1] and ultrafast electron diffraction [2]. In addition to the development of continuous wave electron guns [3, 4], pulsed RF electron gun designs, such as BNL, Tsinghua, and PITZ, are being constantly upgraded [5–7] and have been operated in LCLS [8], FLASH [9], SwissFEL [10], and SXFEL to contribute to research in materials science, medicine, and biology at the atomic and molecular scale [11–13]. However, scientific studies have led to new requests for photoinjectors. First, to obtain a high brightness instrument, the emittance of the electron beam at the exit of the injector must be further reduced. In addition, for better beam quality, the same bunch charge extracted by a shorter laser based on pulse stacking is required to reduce the compression factor [14, 15]. Moreover, current XFEL facilities vary from 700 m to 3 km, so more compact designs are urgently required. Based on photoinjector technology, these requirements cannot be met at the same time. Therefore, a photoinjector with a shorter driven laser and lower emittance as the next generation must be studied for use in advanced facilities.

This work was supported by the National Key R&D Program of China (No. 2018YFF0109203) and ANSO (ANSO-CR-KP-2020-16).

✉ Cheng Wang
wangcheng@sinap.ac.cn

Wen-Cheng Fang
fangwencheng@zjlab.org.cn

Zhen-Tang Zhao
zhaozhentang@sinap.ac.cn

[1] Shanghai Institute of Applied Physics, Chinese Academy of Sciences, Shanghai 201800, China

[2] University of Chinese Academy of Sciences, Beijing 100049, China

[3] Shanghai Synchrotron Radiation Facility, Chinese Academy of Sciences, Shanghai 201204, China

The design of a better photoinjector involves a higher gradient, an emittance compensation design to preserve brightness, and a better cathode to reduce the emittance on the cathode. A high gradient is one of the conditions for excellent accelerator performance that has been explored over the last few decades. Operating photocathode electron guns are based on the L-band (1.3 GHz, 60 MV/m) [16] and S-band (2.856 GHz, 120 MV/m) [17]. One of the methods for increasing the gradient is to increase the frequency because of the well-known theory that the peak accelerating gradient is proportional to the square root of the frequency [18]. Based on operational experience, a C-band gun [19] was designed to operate on a gradient of 150 MV/m in the SXFEL. The X-band gun was designed and tested on a gradient of 200 MV/m at SLAC/LLNL [20].

Previous research on higher achieved gradients shows that cryogenic structures can significantly increase the accelerating gradient using normal conducting technology. In the high-power test of cryogenic X-band structures, a 500-MV/m surface electric field is achieved in standing wave structures [21]. According to material research, the dislocation mobility in the cryogenic structure that corresponds to the breakdown effect is decreased [22]. Moreover, the electrical resistivity of cryogenic copper is lower, and its thermal conductivity is higher [23]. This can lead to a lower heat load on the surface. In addition, an increase in hardness reduces the deformation caused by pulse heating in RF cycles. Cryogenic accelerating structures have been studied as a new and attractive trend at UCLA and LEBRA with corresponding photocathode designs [24, 25]. At CERN, the DC test of the cryogenic structure was recently performed [26]. The cryogenic structure is possibly the main technical route for the next generation of accelerators.

With the promising high gradient and operation experience in the C-band structure, a new cryogenic C-band photocathode electron gun was optimized, fabricated, and tested at low power at SXFEL. Based on the optimized cryogenic photocathode electron gun, some factors that can affect the performance of the gun were analyzed. In the cold test, specific RF properties at room temperature and cryogenic temperature were obtained, which is the foundation of the high-power test and provides a reference for other cryogenic structure designs.

In this paper, optimization of the RF design and cold-test results are presented. In Sect. 3, optimization of the RF design, including parameters such as the local field and multipole mode, are analyzed. In Sect. 4, the sensitivity of the offsets that may affect the beam dynamics is presented. In Sect. 5, the details of the fabrication as well as the cold test at room temperature and cryogenic conditions are presented. The vibration measurements during the test are also described. The cryogenic photocathode electron gun is currently under deployment and will experience a high-power test at SXFEL.

2 RF design and optimization

The cryogenic gun was designed and optimized using SUPERFISH [27] and CST Microwave Studio [28] at room temperature (Fig. 1). In the optimal design, the axial electric field is balanced, the electric field on the surface is lower than the electric field on the cathode, and the mode separation is sufficiently large.

2.1 Suppression of the RF field on the surface

The optimized photocathode electron gun is expected to experience an ultra-high electric field during operation. The estimated 200-MV/m gradient on the cathode may cause breakdown, even under cryogenic conditions. According to research on local field quantity, the risk of RF breakdown in the electron gun can be assessed by means of the modified Poynting vector [29],

$$S_c = Re\{\vec{S}\} + g_c \cdot Im\{\vec{S}\} \quad (1)$$

where $\vec{S}$ is the Poynting vector, g_c is a weighting factor, whereby the performance of structures in a high gradient can be described. In the working mode of the electron gun, the electric field is mostly distributed near the axis, whereas the magnetic field is mostly distributed at the iris. As shown in Fig. 2, a map of S_c in the cross section of the cavity is presented. The S_c parameter is stronger inside the cavity and weaker on the surface. In the S_c simulation, the weighting factor is the typical measured value of 1/6 and is independent of the material parameters.

With a 200-MV/m gradient on the cathode, the maximum modified Poynting vector is 4.73 $W/\mu m^2$. The maximum S_c is located at the cavity wall near the iris. This is because the S_c in the standing wave structures is dominated by the reactive power flow oscillating on each cycle back and forth from the region of the electric field (on the left-hand side) to the region of the magnetic field (on the right-hand side). Because the gun will experience an ultra-high RF field within 2μm and is required to have a BDR below 10^{-6} bpp/s, the calculated S_c may be larger than the limitation of RF structures operating at room temperature. However, for cryogenic structures, smaller dislocations and

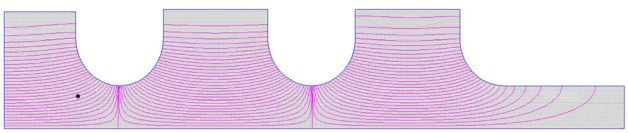

Fig. 1 (Color online) 2.6-cell C-band gun profile

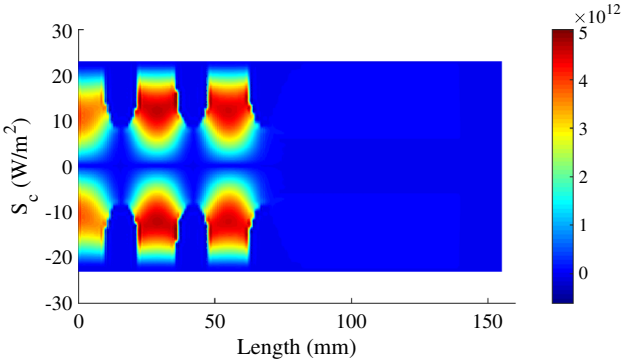

Fig. 2 (Color online) Distribution of the local field quantity S_c in the cavity at a gradient of 200 MV/m. The maximum value was 4.73, located near the iris

deformation may improve the limits of S_c. When conducting high-power experiments under cryogenic conditions, the theory of a high gradient at low temperatures can be further validated using the achievable maximum gradient. The RF properties of the optimized cryogenic RF gun are listed in Table 1.

2.2 Optimization and elimination of multipole mode

The photoinjector is composed of a cryogenic electron gun, solenoids, and C-band traveling wave sections. At the optimum working point, the photoinjector can produce a low-emittance electron beam using a short driven laser. The performance of the photoinjector is listed in Table 2.

A coaxial coupler was designed for RF measurements and operation at room temperature. The structural design of the coupler is based on a C-band rectangular waveguide, so that the multipole mode, which can affect the beam quality, may exist in the cavity. To investigate the influence of the multipole component on the beam quality in the cavity field, the field along a small circle around the beam axis in each cell is shown in Fig. 4b.

Table 1 Optimized 2.6 cell gun

Condition	Room	Cryogenic
Frequency π mode (MHz)	5692.9	5712
Frequency $\pi/2$ mode (MHz)	5674.5	5693.6
Frequency 0 mode (MHz)	5647	5666
Q_0	9850	54000
Shunt impedance (MΩ)	6.285	34.455
E_z, cathode (MV/m)	200	
E_{max}/E_{acc}	0.917	
Peak RF power (MW)	16.773	3.07
Max S_c (W/μ m^2)	4.73	
RF pulse length (μs)	2	
Maximum RF pulse heating (K)	75.45	7.8

Table 2 Optimized performance for the cryogenic C-band injector

Parameters	Values
Bunch charge (pC)	500
Laser Pulse FWHM (ps)	5
RMS laser size (mm)	0.354
Launching phase (°)	46
Emittance on the cathode (mm·mrad)	0.212
Beam energy (MeV)	107.3
Transverse emittance (mm·mrad)	0.2875
RMS bunch length (mm)	0.465
Mean slice emittance (mm·mrad)	0.22
Relative RMS energy spread	0.73%

The multipole mode obtained by the simulation when using the coaxial coupler is not strong, because the box part of the coaxial coupler has the effect of eliminating the dipole mode. Thus, a weak dipole mode is observed in the cell near the coaxial coupler, and it is weaker in the other two cells. The effect of this dipole mode on the emittance can be estimated using the equation:

$$\Delta\epsilon_y = \frac{eE_0L}{2mc^2} \times na_n r^{n-1}\sigma_y\sigma_z, \tag{2}$$

where n is half of the multipole order, L is the full-cell length, σ is the RMS bunch size of the other two dimensions, and a_n is the Fourier coefficient of the multipole mode obtained by fitting from the extracted field [30]. With the parameters $r = 1$ mm and $L = 26.3$ mm, the unexpected emittance growth caused by the dipole mode is 0.027 mm·mrad. The injector was optimized using a multi-objective evolutionary algorithm. At 500 pC and a 5-ps initial bunch, the emittance without any asymmetry introduced is 0.2875 at the selected working point. Therefore, the effect of this dipole mode component on the total emittance in the side cell does not exceed 5%. The estimated emittance growth in the middle cell and cathode cell did not exceed 0.1% because of the lower multipole mode component.

3 Effects of alignment tolerance and RF jitter on emittance growth

Alignment deviation and RF jitter are the primary sources of emittance growth. The deviation of each element in the injector causes asymmetry during electron beam operation. Thus, the disturbance caused by the

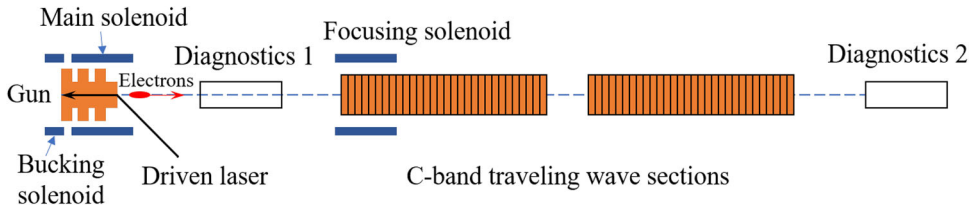

Fig. 3 (Color online) Layout of the C-band photoinjector

alignment deviation and RF jitter must be analyzed by simulation. These unexpected errors need to be analyzed for the injector to produce a consistently high-quality beam.

The beam performance affected by the offsets was simulated using ASTRA [31]. In the simulation, the optimized working point was used as the reference point, and only one component was perturbed at a time.

Because of the possible jitter in the control system, the amplitude of the gradient on the cathode and the arrival time related to the launch phase may vary. These jitters not only cause small changes in beam energy, but also shift the working state away from the working point, thus causing additional emittance growth. In the simulation, the variation of the emittance with the RF amplitude and RF launch phase in the gun cavity was studied. As shown in Fig. 5, the offset of the RF amplitude was set to 1 MV/m, and a lower emittance value existed on the higher gradient side. Within the bias range, the maximum effect of the RF amplitude on the emittance was 17%. The offset of the RF phase was set within 1° RF, corresponding to a 480-fs laser arrival time. In this offset range, the variation in emittance is less than 0.005 mrad, which is less than 2%. In the operation, the offset in RF amplitude is 0.04%, corresponding to 0.08 MV/m, which is 0.18% in the RF phase. In this region, the designed photoinjector showed acceptable emittance growth.

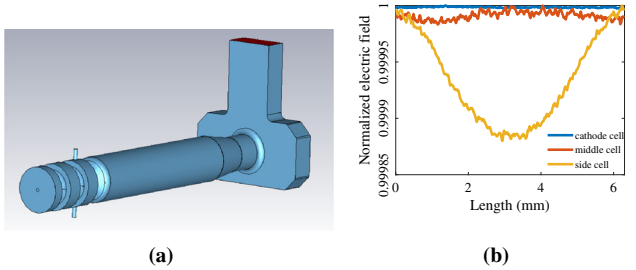

Fig. 4 (Color online) Design of the coupler based on coaxial waveguide **a** and the multipole mode along a small circle around the beam axis in each cell **b**

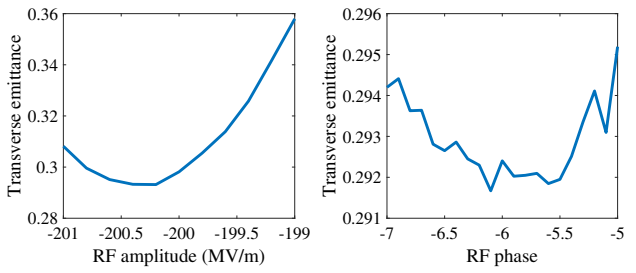

Fig. 5 (Color online) Bunch emittance growth as a function of RF amplitude (left) and the launch phase (right). Note that the launch phase is with respect to the maximum energy gain

In addition, the solenoids may be offset in both the transverse and longitudinal directions because of alignment and installation errors. The transverse offset of the solenoid causes the electron beam to experience an asymmetric magnetic field, while the longitudinal offset of the solenoid will cause the integral field of the magnetic field experienced by the beam to differ from the working point. Within 1 mm displacement in the vertical direction, the transverse emittance increases to 0.85 mm-mrad in the vertical direction and to 0.55 mm-mrad in the horizontal direction from 0.2875 mm·mrad. A longitudinal offset of 5 mm will cause an additional emittance of up to 0.41 mm·mrad. However, with the current technology, the alignment accuracy of 0.1 mm in the transverse direction can be achieved. Within 0.1 mm, the offset of the solenoid in the transverse and longitudinal directions only has a minor effect on the emittance growth.

Moreover, the beam quality is also affected by deviations in the laser incidence and displacement of the electron gun cavity. This is due to the error in the position of the laser and cavity, causing the jitter in the relative position of the beam with respect to the acceleration field. This error results in an off-axis beam and causes emittance growth. As shown in Fig. 7, the simulated emittance varies with the laser center and gun cavity. In the simulation, the positions of the other components remained unchanged, and the offsets were only applied to the electron gun and the drive laser. The maximum emittance is 1.5 mm·mrad within a 1 mm vertical offset of the drive laser. An offset in the electron gun can cause the electron beam to experience an asymmetric field only within the electron gun, whereas an offset in the driving laser will cause the beam to experience an asymmetric field throughout the entire injector, including the electron gun, solenoid, and traveling

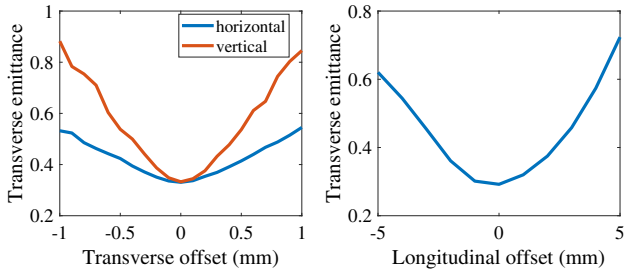

Fig. 6 Bunch emittance growth as a function of the transverse (left) and longitudinal (right) offset of the solenoid

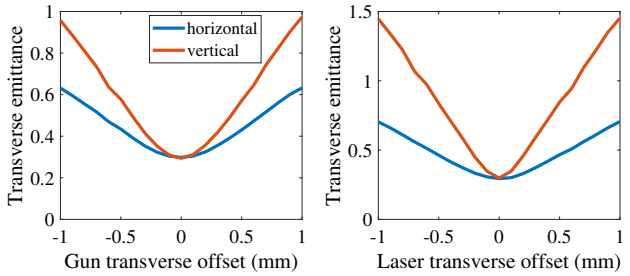

Fig. 7 (Color online) Bunch emittance growth as a function of the gun transverse (vertical) offset (left) and the driven laser vertical offset (right)

wave sections. Technically, the laser can be accurate to 0.1 mm, in which case the emittance growth becomes acceptable.

Based on the above discussion and simulations, the changes in emittance with various effects are summarized in Table 3.

4 Manufacture and RF tuning

The electron gun was fabricated and installed on the cryogenic platform at SXFEL. The gun cavity was designed with a 2.6-cell structure. For such a high gradient, a 2.6-cell electron gun can accelerate the electrons to the energy region near the velocity of light. A sectional view of

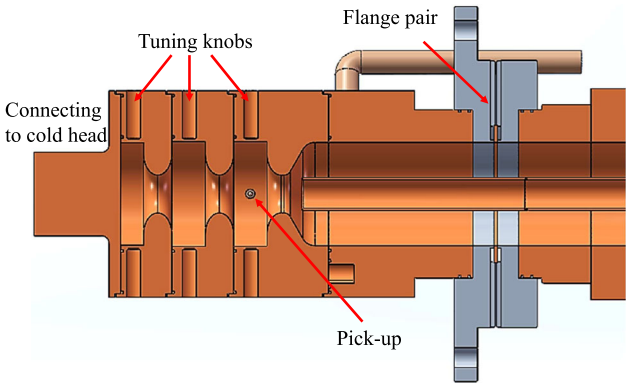

Fig. 8 (Color online) Mechanical design of the gun cavity

the electron gun is shown in Fig. 8. In addition to the external cooling system (cryogenic platform), there is also a water-cooling circuit buried inside the copper in the design for operation at room temperature. Tuning knobs are designed on each cavity to compensate for frequency detuning resulting from various mechanical errors. The pick-up is located at the cell near the mode launcher.

As an alternative design, the gun cavity and couplers attached to the mode launcher were processed separately. During the fabrication process, each cell of the cavity was manufactured individually. The dimensions of the cavity are strictly in accordance with the simulation results, with a tolerance of no more than 5μm.

4.1 Low-power RF test at room temperature

To ensure mechanical working precision, microwave measurements were performed before diffusion bonding. As shown in Fig. 9, in an atmospheric environment of 15 °C, the resonant frequencies are 5647.125, 5674.594, and 5693.1 MHz, very close to the design frequency. For better thermal transfer performance, the cathode was brazed directly into the cavity in this design. Gold-copper welding wire was used, and brazing was performed under the protection of hydrogen to keep the surface of the structure clean. After diffusion bonding, the resonant frequencies increased to 5647.9, 5675.6, and 5694 MHz, the Q factor at

Table 3 Variation in emittance caused by imperfections

	Introduced disturbance	Emittance (mm·mrad)
Optimized emittance		0.2875
Multipole mode		0.289
RF amplitude	1 MV	0.3579
RF phase	1 deg	0.2952
Solenoid offset (tran)	1 mm	0.88
Solenoid offset (long)	5 mm	0.72
Gun transverse offset	1 mm	0.97
Laser transverse offset	1 mm	1.45

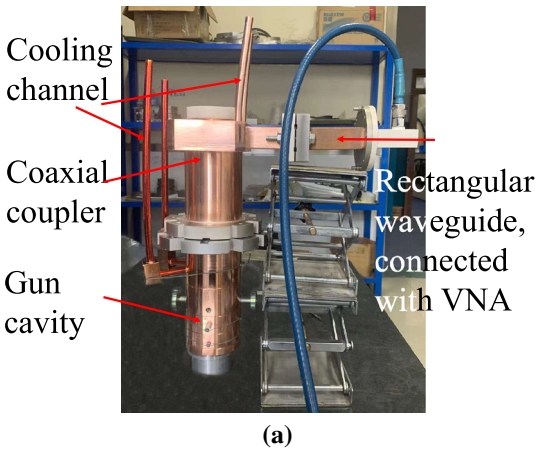

(a)

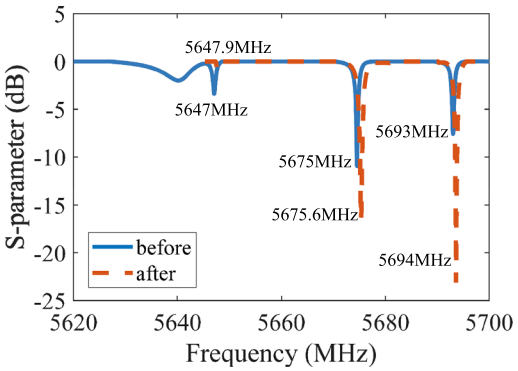

(b)

Fig. 9 (Color online) Low-power RF test of the electron gun at room temperature (**a**). *S*-parameters before and after diffusion bonding (**b**)

the working frequency increased to 9600 from 8300, and the reflection of each mode changed differently.

The cold test was performed in an atmospheric environment with an ambient temperature of 298 K. Considering the temperature correction and atmospheric pressure, the frequency of the working mode in the cold test should be 5691 MHz. Thus, the cavity was tuned to obtain a balanced field at the design frequency. As there is no hole in the middle of the cathode, the bead-pull perturbation for the on-axis field distribution measurement was performed with a 3-mm-diameter steel bead at room temperature. The bead descended very slowly from the exit of the beam and stopped at the cathode. During the RF tuning, some problems occurred, and the gun cavity was not tuned to its design frequency. After tuning, the cavity frequency was 5693 MHz, and the field distribution was not perfectly balanced. However, the field distribution in Fig. 10, which is an averaged result of five runs of the measurements, shows that the balance of the field is 1.12. The field was stronger in the cathode and middle cells. The current on-axis field distribution is capable of RF cold tests and high-

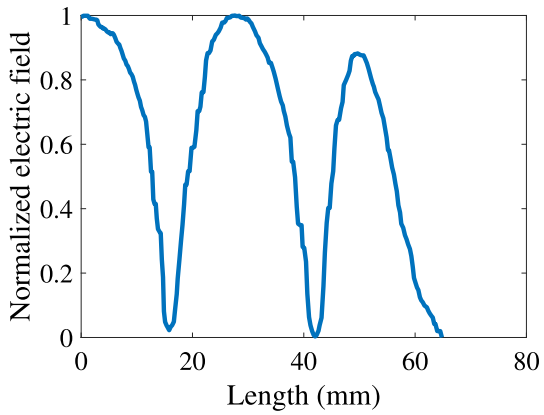

Fig. 10 Axial field distribution with the bead pull method. The field balance is 1.12

power experiments, and we will tune the cavity further at room temperature in subsequent work.

4.2 RF cold test in the cryostat

The cryogenic test of the electron gun was performed on the cryogenic platform. As shown in Fig. 11a, the gun cavity was inverted, and the cathode side was connected to the second-stage cold head of the cryocooler via a reserved inset structure. In the cryogenic test, the gun cavity was tested using a vector network analyzer. To save space and facilitate mechanical design, a coupler based on a circular waveguide was used for cryogenic testing in a cryostat. The power was transmitted through the rectangular waveguide and the circular mode launcher, finally reaching the gun cavity. The vacuum requirements of the cryogenic platform are 10^{-6} Pa at room temperature and 10^{-7} Pa at cryogenic temperatures, provided by a molecular pump and an ion pump. This is one of the bases of high-power experiments.

The cooling process lasted for 30 h, and the temperature of the electron gun was reduced from 283 K. When the cryocooler was in operation, the dynamic RF properties of the electron gun with temperature were obtained. After 30 h, the temperature of the gun cavity stabilized at 42.5 K, while the temperature of the cooling head was 19.3 K. As shown in Fig. 12, the frequency increased to 5713.64 MHz from 5695.4 MHz at 283 K. In addition to frequency, characterizing the coupling coefficient and Q factor is the main objective of the cryogenic test. In this test, the behavior of the coupling coefficient and Q factor were evaluated from the S-parameter using the following equation:

$$Q_0 = \sqrt{\frac{(\beta\rho_x - 1)(\rho_x - \beta)}{\rho_x}}\frac{f_0}{f_{x2} - f_{x1}}, \tag{3}$$

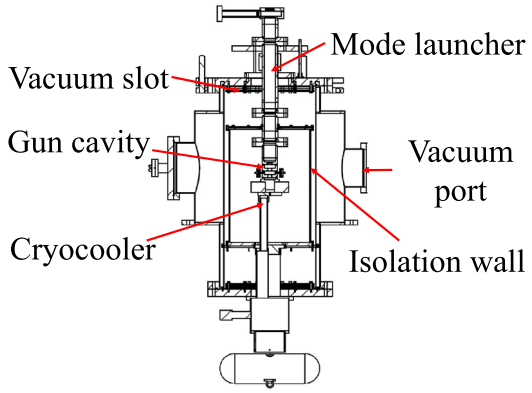

(a)

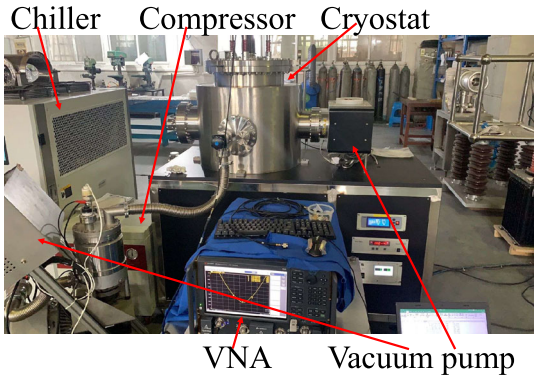

(b)

Fig. 11 (Color online) Mechanical design of the cryogenic test platform (**a**). The cathode side of the gun cavity is connected to the second-stage cooling head. Photograph of cryostat during cryogenic test (**b**)

where the coefficient is obtained from the standing-wave ratio. As the frequency increases with decreasing temperature, the coupling coefficient increases to 3.1 from 0.78, and the Q factor increases to 45300 from 9800. The coupling coefficient and Q factor vary by essentially the same factor, and the results are in good agreement with the theory of cryogenic structures. In the cryogenic test, the lowest temperature reached by the gun cavity did not reach the design value of 20 K. It is assumed that this occurred, because the gun cavity did not come into full contact with the second-stage cold head during assembly. In addition, the frequency reached in the cryogenic test was 1.6 MHz higher than the design value. The deviation in frequency can be compensated by changing the operating temperature. The electron gun was reassembled on the cryogenic test platform after tuning.

4.3 Vibration measurement and analysis

During the cryogenic test, a twitch at a frequency of approximately 3 kHz was observed, even after the cavity reached a stable temperature. It is estimated that this twitch comes from the mechanical vibrations on the cavity; thus, the vibration was measured on the cavity and the surroundings while the cryogenic platform was operational. The representative points chosen for the vibration measurements were on the ground, on the cryostat, and near the cathode of the gun cavity. In the measurement, velocity sensors were used to collect the displacement signal at each moment, and the vibration signal in the time domain was transformed into the frequency domain by means of a Fourier transform. The vibration measurements lasted for 1 h. As presented in Fig. 13, the displacement power spectral density shows that the recorded vibration is mostly at 1 Hz, and the rest are harmonics. The RMS vibration displacements are presented in Table 4. The maximum RMS vibration of 53μm occurred on the cavity, while the RMS displacements in the other two directions were 9μm and 7μm.

The results of the experiment discussed above suggest that the electron gun is simultaneously subjected to random ground vibrations, vibrations from refrigeration equipment

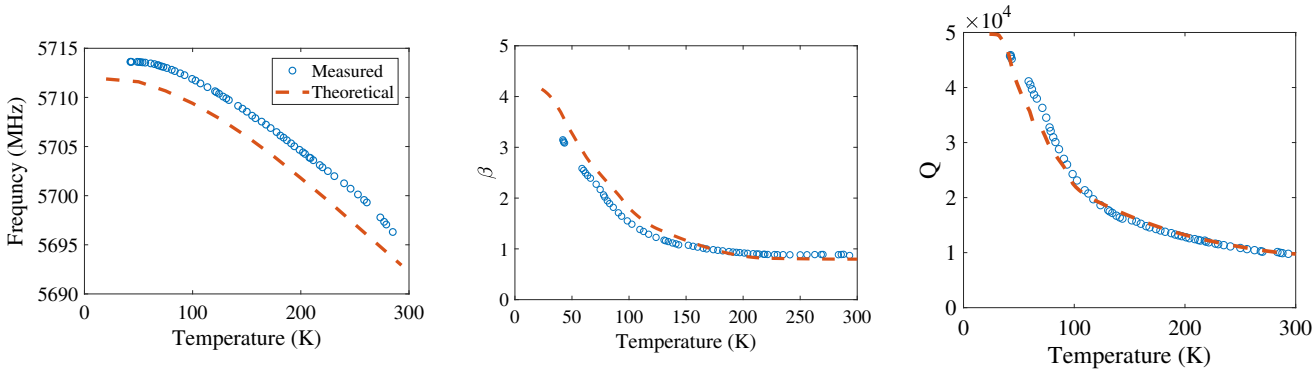

Fig. 12 (Color online) Results of the cryogenic cold-test. The frequency increased from 5695.4 MHz to 5713.6 MHz (left) while the temperature varied from 286 K to 42 K. An increase in the coupling coefficient (middle) and quality factor (right) was observed

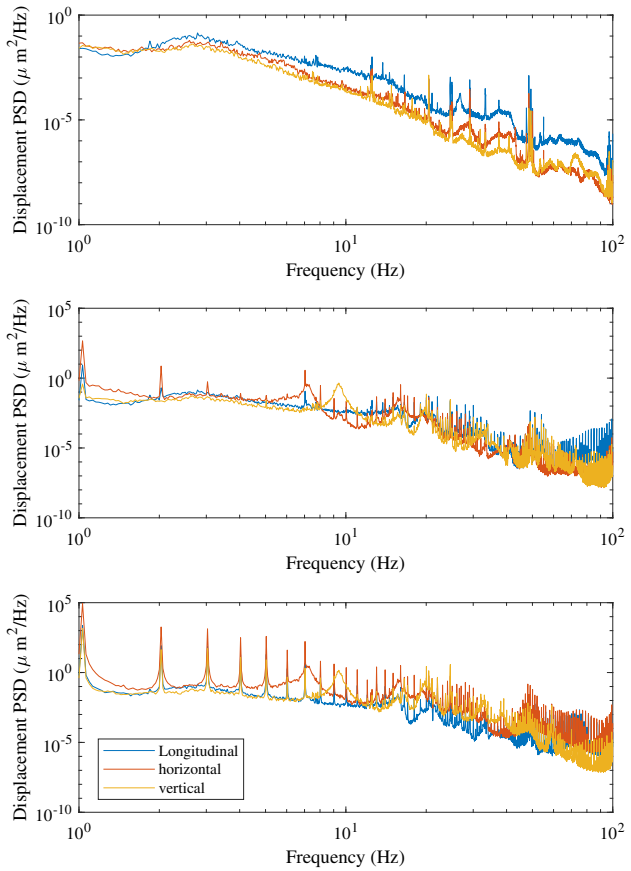

Fig. 13 (Color online) Measured vibration spectra during cryocooler operation. The top graph shows the data collected on the ground, the middle graph is that on the cryostat, and the bottom graph shows the vibration data collected on the gun cavity. Vibrations of 1 Hz from the cryocooler were observed in the cavity

and vacuum equipment, and periodic vibrations of other equipment in the environment. The vibrations occur primarily in the section plane of the cryocooler, which is caused by the periodic motion of the original parts inside the cryocooler. In addition, the test platform is not rigidly connected to the ground, causing large displacements on the test platform when subjected to forced vibrations. However, this test was performed in a complicated environment, and vibration isolation was not optimized. The current measurement presents the basis of the situation. With a 50-μm vibration, the increase in emittance is no more than 4%, referring to the simulation results above. In future research, the cryogenic platform will be upgraded to include design considerations such as vibration isolation and ground fixation.

After the tuning process, the electron gun in the cryogenic test platform underwent a high-power test. The high-power test platform was based on that at SXFEL [32]. The layout of the power transmission system is shown in Fig. 14. The cryogenic test platform was connected downstream of the entire system. In the high-power test, the RF source was a 50-MW C-band klystron. The repetition rate was 10 Hz. The power generated by the klystron is transmitted through the rectangular waveguide, divided by the power splitter [33], and finally reaches the cryogenic platform. In this system, a circulator is used to prevent power reflection, which can break the klystron. In the high-power test, the maximum achievable gradient and breakdown rate are picked up by the port with the antenna on the cavity. Currently, a high-power test platform is used for high-power experiments of a room-temperature C-band photocathode gun. The high-power experimental results of the cryogenic gun will be a foundation for the further design of cryogenic structures. Based on the high-power test platform, the entire photoinjector will be tested in the phase II plan, aiming to produce a high-quality beam from a cryocooled cathode and cryogenic RF gun.

5 Discussion

The cryogenic electron gun is operated at a low temperature of 20−77 K using normal conducting technology. The ability of the cryogenic electron gun to achieve extremely high accelerating gradients makes it suitable for future ultra-compact injectors. The cryogenic electron gun can produce a low-emittance electron beam with a short driven-laser pulse. In contrast to the traditional model, the variation of RF parameters such as frequency with temperature must be considered in the design of the cryogenic electron gun. Moreover, a high-power experiment is

Table 4 RMS Vibration in the cryogenic test

	Longitudinal (μm)	Horizontal (μm)	Vertical (μm)
On the ground	0.4684	0.3426	0.2901
On the cryostat	0.7465	3.9236	0.6129
On the cavity	8.9356	53.1349	7.1549

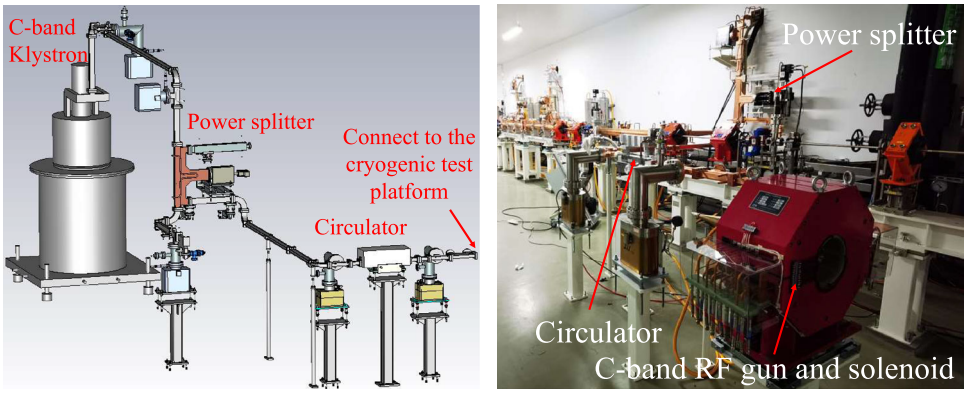

Fig. 14 (Color online) High-power test platform, including a C-band klystron, an adjustable power slitter, and the circulators. Currently, the high-power test platform is used for high-power experiments with a room-temperature C-band photocathode gun

required to confirm the achievable stable accelerating gradient.

6 Conclusion

In this paper, the results of an RF cold test and cryogenic test of an electron gun are presented. Considering breakdown verification, dipole mode evaluation, and offset simulation, the design presented here for a cryogenic electron gun can maintain stable operation. In the cold test, the gun frequency and field distributions were obtained. The variation of RF properties with temperature was determined, which is generally consistent with the simulation. The test results are the foundation of high-power experiments and other cryogenic normal-conducting accelerating structures.

In a subsequent study, the gun cavity will be tuned to reach the working frequency and balance the field distribution. Moreover, vibration isolation will be taken into consideration in the upgrade of the new cryogenic system, which can be integrated around the electron gun. Therefore, the new cryogenic electron gun will produce a high-quality beam stably at the designed temperature.

Authors' contributions All authors contributed to the study conception and design. Material preparation, data collection and analysis were performed by Cheng Wang, Jian-Hao Tan, Xiao-Xia Huang and Yi-Xing Lu. The first draft of the manuscript was written by Cheng Wang and all authors commented on previous versions of the manuscript. All authors read and approved the final manuscript.

References

1. M.P. Minitti, J.M. Budarz, A. Kirrander et al., Imaging molecular motion: femtosecond x-ray scattering of an electrocyclic chemical reaction. Phys. Rev. Lett. **114**, 255501 (2015). https://doi.org/10.1103/PhysRevLett.114.255501
2. S. Weathersby, G. Brown, M. Centurion et al., Mega-electron-volt ultrafast electron diffraction at slac national accelerator laboratory. Rev. Sci. Instrum. **86**, 073702 (2015). https://doi.org/10.1063/1.4926994
3. C. Wang, Z.H. Zhu, Z.G. Jiang et al., Design of a 16.25 mhz continuous-wave normal-conducting radiofrequency electron gun. Nucl. Sci. Tech. **31**, 110 (2020). https://doi.org/10.1007/s41365-020-00817-3
4. K. Liu, L. Li, C. Wang et al., Multi-port cavity model and low-level rf systems design for vhf gun. Nucl. Sci. Tech. **31**, 8 (2020). https://doi.org/10.1007/s41365-019-0711-2
5. J.F. Schmerge, J. Castro, J.E. Clendenin et al., The s-band 1.6 cell rf gun correlated energy spread dependence on π and 0 mode relative amplitude. Int. J. Modern Phys. A **22**, 4061–4068 (2007). https://doi.org/10.1142/S0217751X07037639
6. D. Ying-Chao, Y. Li-Xin, D. Qiang et al., First beam measurements of the s-band photocathode radio-frequency gun at tsinghua university. Chin. Phys. Letts. **24**, 1876–1878 (2007). https://doi.org/10.1088/0256-307x/24/7/024
7. Y. Chen, H.J. Qian, M. Krasilnikov et al., Frequency-detuning dependent transient coaxial rf coupler kick in an l-band long-pulse high-gradient rf photogun. Phys. Rev. Accel. Beams **23**, 010101 (2020). https://doi.org/10.1103/PhysRevAccelBeams.23.010101
8. W.E. White, A. Robert, M. Dunne, The linac coherent light source. J. Synchrotron Radiat. **22**, 472–476 (2015). https://doi.org/10.1107/s1600577515005196
9. J. Feldhaus, Flash-the first soft x-ray free electron laser (fel) user facility. J. Phys. B Atomic Mole. Optical Phys. **43**, 194002 (2010)
10. R. Ganter, *Swissfel-Conceptual Design Report* (Tech. rep Paul Scherrer Institute (PSI), Villigen, 2010)
11. C. Feng, H.X. Deng, Review of fully coherent free-electron lasers. Nucl. Sci. Tech. **29**, 160 (2018). https://doi.org/10.1007/s41365-018-0490-1
12. H.P. Geng, J.H. Chen, Z.T. Zhao, Scheme for generating 1 nm x-ray beams carrying orbital angular momentum at the sxfel. Nucl. Sci. Tech. **31**, 88 (2020). https://doi.org/10.1007/s41365-020-00794-7
13. X. Li, J.Q. Zhang, G.Q. Lin et al., Performance of an electron linear accelerator for the first photoneutron source in China. Nucl. Sci. Tech. **30**, 53 (2019). https://doi.org/10.1007/s41365-019-0576-4
14. B.J. Claessens, S.B. van der Geer, G. Taban et al., Ultracold electron source. Phys. Rev. Lett. **95**, 164801 (2005). https://doi.org/10.1103/PhysRevLett.95.164801
15. S. Bettoni, M. Aiba, B. Beutner et al., Preservation of low slice emittance in bunch compressors. Phys. Rev. Accel. Beams **19**, 034402 (2016). https://doi.org/10.1103/PhysRevAccelBeams.19.034402

16. M. Altarelli, R. Brinkmann, M. Chergui et al., The european x-ray free-electron laser. Tech. Design Report DESY **97**, 1–26 (2006). https://doi.org/10.1080/08940880601064968
17. R. Akre, D. Dowell, P. Emma et al., Commissioning the linac coherent light source injector. Phys. Rev. Accel. Beams **11**, 030703 (2008). https://doi.org/10.1103/PhysRevSTAB.11.030703
18. W. Kilpatrick, Criterion for vacuum sparking designed to include both rf and dc. Rev. Sci. Instrum. **28**, 824–826 (1957). https://doi.org/10.1063/1.1715731
19. W. Fang, L. Wang, Z. Zhao, Conceptual study and design of a c-band photocathode injector. Radiat. Detect. Technol. Methods **3**, 39 (2019). https://doi.org/10.1007/s41605-019-0117-z
20. C. Limborg-Deprey, C. Adolphsen, D. McCormick, et al., Performance of a first generation x-band photoelectron rf gun. Phys. Rev. Accel. Beams. **19**, 053401 (2016). https://doi.org/10.1103/PhysRevAccelBeams.19.053401
21. A.D. Cahill, J.B. Rosenzweig, V.A. Dolgashev et al., High gradient experiments with *x*-band cryogenic copper accelerating cavities. Phys. Rev. Accel. Beams **21**, 102002 (2018). https://doi.org/10.1103/PhysRevAccelBeams.21.102002
22. E.Z. Engelberg, Y. Ashkenazy, M. Assaf, Stochastic model of breakdown nucleation under intense electric fields. Phys. Rev. Letts. **120**, 124801 (2018). https://doi.org/10.1103/PhysRevLett.120.124801
23. N.J. Simon, E.S. Drexler, R.P. Reed, Properties of copper and copper alloys at cryogenic temperatures. Final report. United States: N. p. (1992). https://www.osti.gov/biblio/5340308
24. J.B. Rosenzweig, A. Cahill, V. Dolgashev et al., Next generation high brightness electron beams from ultra-high field cryogenic radiofrequency photocathode sources. Phys. Rev. Accel. Beams **22**, 023403 (2019). https://doi.org/10.1103/PhysRevAccelBeams.22.023403
25. A. Iino, S. Yamaguchi, T. Shintomi et al., Development of low-loss cryo-accelerating structure with high-purity copper. Nucl. Instrum. Meth. A **866**, 40–47 (2017). https://doi.org/10.1016/j.nima.2017.04.012
26. H. Lee, I. Bazarov, L. Cultrera, A cryogenically cooled high voltage dc photogun. in Proceedings of IPAC2017, Copenhagen, Denmark, 1618–1621 (2017)
27. K. Halbach, R. Holsinger, Superfish—a computer program for evaluation of rf cavities with cylindrical symmetry. Particle Accel. **7**, 213–222 (1976)
28. Cst studio suite, cst mircowave studio. https://www.3ds.com/products-services/simulia/products/ststudio-suite/
29. A. Grudiev, S. Calatroni, W. Wuensch, New local field quantity describing the high gradient limit of accelerating structures. Phys. Rev. Accel. Beams **12**, 102001 (2009). https://doi.org/10.1103/PhysRevSTAB.12.102001
30. M.S. Chae, J.H. Hong, Y.W. Parc et al., Emittance growth due to multipole transverse magnetic modes in an rf gun. Phys. Rev. Accel. Beams **14**, 104203 (2011). https://doi.org/10.1103/PhysRevSTAB.14.104203
31. K. Floettmann, Astra, a space charge tracking algorithm. http://www.desy.de/mpyflo/
32. C.C. Xiao, J.Q. Zhang, J.H. Tan et al., Design and preliminary test of the llrf in c band high-gradient test facility for sxfel. Nucl. Sci. Tech. **31**, 100 (2020). https://doi.org/10.1007/s41365-020-00806-6
33. Z.B. Li, A. Grudiev, W.C. Fang et al., Radio-frequency design of a new c-band variable power splitter. Nucl. Sci. Tech. **30**, 100 (2019). https://doi.org/10.1007/s41365-019-0611-5